Journal Name

RSCPublishing

ARTICLE

2D and 3D Vanadium Oxide Inverse Opals and Hollow Sphere Arrays

Cite this: DOI: 10.1039/x0xx00000x

Eileen Armstrong, Michal Osiak, Hugh Geaney, Colm Glynn, and Colm O'Dwyer*

Received 00th January 2012,
Accepted 00th January 2012

DOI: 10.1039/x0xx00000x

www.rsc.org/

High quality 2D and 3D inverse opals and hollow sphere arrays of vanadium oxide are grown on conductive substrates from colloidal polymer sphere templates formed by electrophoretic deposition or surfactant-assisted dip-coating. Inverse opals (IOs) are formed using variants of solution drop-casting, N_2-gun assisted infiltration and high-rate (200 mm/min) iterative dip-coating methods. Through Raman scattering, transmission electron microscopy and optical diffraction, we show how the oxide phase, crystallinity and structure are inter-related and controlled. Opal template removal steps are demonstrated to determine the morphology, crystallinity and phase of the resulting 2D and 3D IO structures. The ability to form high quality 2D IOs is also demonstrated using UV Ozone removal of PMMA spheres. Rapid hydrolysis of the alkoxide precursor allows the formation of 2D arrays of crystalline hollow spheres of V_2O_5 by utilizing over-filling during iterative dip-coating. The methods and crystallinity control allow 2D and 3D hierarchically structured templates and inverse opal vanadium oxides directly on conductive surfaces. This can be extended to a wide range of other functional porous materials for energy storage and batteries, electrocatalysis, sensing, solar cell materials and diffractive optical coatings.

INTRODUCTION

Photonic Crystals (PhCs),[1] the basis for many of nature's colour schemes (butterfly wings, dragonflies, beetles etc.),[2] have proven highly useful for many applications throughout optics and optoelectronics.[3, 4] Artificial PhCs, formed through the self-assembly of silica or polymer spheres (PS, PMMA), are becoming widely accepted as low cost and stable templates for the formation of three-dimensional (3D) and two-dimensional (2D) ordered structures.[5-8] for example, Waveguides,[9] optical switches,[10] and light-emitting devices[11] with enhanced output power and external quantum efficiency have all been successfully produced using artificial opal templates. A growing area of interest however, is the potential these structures hold for the formation of three-dimensionally ordered macroporous (3DOM) or inverse opal battery electrodes.[12-14] Inverse opals, as the name suggests, are formed by the infiltration of a PhC template or artificial opal with a material precursor and removal of the template. These structures have the advantage of periodicity in all three dimensions and the consequent possibility for a full photonic bandgap. These structures therefore, through template design and choice of infill material, allow the optical characteristics or phenomena of a material system to fit the desired application. The variety of assembly routes[15] available for the formation of these templates, such as spin coating,[16] drop casting,[17] electrophoretic deposition,[18] Langmuir-Blodgett,[19] vertical deposition or dip coating,[20, 21] make it a well-controlled and easily adapted method for template design and formation.[22]

The open and interconnected architectures have been shown to improve battery performance through increased conductivity and better electrolyte infiltration, providing substantial improvements in both power and rate capabilities.[13, 23] These properties have also been shown to extend to electrocatalysts, allowing a hierarchically porous host structure that incorporates efficient catalytic nanocrystals.[24, 25] IO structures could provide that continuously sought after duplex of abilities; the battery that not only stores large amounts of energy in a light weight, binder free mouldable material can exhibit the power density capabilities of super-capacitors with the energy density of Li-ion batteries, required by the growing number of high power applications.[14, 26-30] Controlled porosity in functional materials has been continuously pursued for a wide range of materials in an effort to understand their synthesis, crystallization and their properties.[31-33]

Vanadium oxides, in their various phases, have been employed in catalysis, energy storage and supercapacitors,[10, 34, 35] photovoltaics,[36] thermochromic and electrochromic devices,[37-41] as well as sensing[42, 43] and field emission devices.[44, 45] Developing methods towards structuring vanadium oxide into ordered and optically significant architectures has the potential therefore to advance several types of functional devices. Vanadium oxide has long been a potential replacement cathode material for use in rechargeable lithium ion batteries due primarily to its layered geometry for cation intercalation, high theoretical specific capacity and low cost.[46-49] Silver vanadium oxides are the primary materials for medical device batteries.[50, 51] When the c-axis of its unit cell structure is minimized, it has been shown to withstand high rates of intercalation allowing fully reversible charge discharge performance.[52-54] Most recently, it has proven successful for use in sodium ion batteries, a potential alternative to Li-ion technologies.[55] Some success has been made in combining the structural advantages of the 3-dimensionally ordered macroporous (3DOM) architecture with V_2O_5 to form a continuous network of porous V_2O_5 material with the aim of tackling the limited electronic conductivity issue faced by most V_2O_5 materials. Recent alternative methods have successfully demonstrated how mesocrystals of V_2O_5 can form using liquid crystals-based phases known as tactosols.

Vanadium oxide inverted opals (IOs) have primarily been formed as non-crystalline aerogel vanadium oxide synthesized from precursor infiltration and solvent exchange methods. Investigations in using electrodeposited crystalline V_2O_5 have also been made, quite often concentrating on electrochromic performance in 3D IOs.[56, 57] Recently, a thin layer of V_2O_5 was successfully electrodeposited on a 3D aluminum electrode for application as a Li-ion microbattery.[58] Controlling the phase, crystallinity and order in high quality IOs is critical for correlating structural changes, material and interface composition, electrochemical activity and electrical connection. In optical applications, the requirements for a high degree of order in the crystalline material would benefit from improvements in the methods of their synthesis and formation. Control in under- and over-infiltration methods by altering the influence of strong capillary forces through lowered viscosity and dip-coating for example, also provide opportunities for inverse opals as well as close-packed arrays of hollow spheres. Amorphous 2D structures can demonstrate controlled lasing and somewhat ordered 3D arrays can realize colour arrays independent of reflection angle for example.

Here, we present several routes for crystalline or amorphous 2D and 3D V_2O_5 inverse opals and hollow sphere arrays by low temperature crystallization of liquid precursor infiltrated colloidal crystal opal templates formed by electrophoretic deposition. Two alternative methods of precursor infilling are demonstrated and thickness disparities and morphological variations are distinguished by particularly distinct Raman scattering responses and crystalline quality after equal heat treatments. The investigations uncover the specific phase transitions occurring during 3D IO formation. Methods towards the formation of amorphous and crystalline 2D V_2O_5 IOs on conductive substrates are also outlined.

EXPERIMENTAL

Materials and Substrates

Polystyrene (PS) spheres, 500 nm in diameter and functionalized with sulphate ion for increased negative charge, were purchased from Polysciences Inc. in 2.5 wt% aqueous solutions and used as received. Poly(methylmethacrylate) (PMMA) spheres, 700 nm in diameter, were prepared with altered concentrations by the emulsion polymerization procedure as described by Schroden, centrifuged and re-suspended in distilled water to form a 5 wt% aqueous solution. Ammonium hydroxide 30% aqueous (NH_4OH) and the surfactant sodium dodecyl sulphate (SDS) were used as received from Sigma Aldrich.

Two types of substrates were used. Silicon wafer, cut into approximately 20 mm × 1 mm pieces, was cleaned in argon plasma and coated with a 10 nm titanium adhesion layer and 100-150 nm gold by ion beam sputtering using an ATC Orion-5-UHV sputtering system. Indium tin oxide (ITO) coated glass was purchased from Sigma Aldrich and cut to approximately 8 × 25 mm pieces. Both types of substrate were cleaned by sonication in acetone, isopropanol (IPA) ethanol and deionized water.

Template Formation (3D and 2D)

Multi-layered colloidal crystal templates using the sulphated PS spheres were formed on the ITO coated glass by electrophoretic deposition (EPD). This was performed, similarly to the method described by Rogach *et al.*,[18] in a cylindrical glass cell, with the ITO glass as the vertical anode and a stainless steel sheet as the counter electrode, held approximately 5 mm away from and directly in parallel with the anode. The solution was prepared using 0.8 mL of the 2.5 wt% sulphated PS solution mixed with 4.3 mL ethanol, and ~ 80 µL of 30% aqueous NH_4OH to ensure a pH of between 8 and 10. This produced a final concentration of spheres of ~0.4%. The electrophoretic deposition was carried out at 3 V for 10 min. Monolayer templates of PMMA spheres on gold coated silicon, were formed by the method outlined in our previous work,[21] whereby the surfactant SDS was added to the solution of PMMA spheres, at a concentration of 8 mg mL^{-1}, this is above the theoretical critical micelle concentration (CMC) for SDS of 2.3 mg mL^{-1} (8.0×10^{-3} mol dm^{-3}). The substrate was then settled vertically in the solution and removed at a rate of 1 mm mL^{-1} using an MTI Corporation PTL-MM01 Dip Coater apparatus. All templates were dried in air but heated further before infilling for ~2 h at a lower temperature of 50-70 °C to enhance unification.

Fabrication of Inverted Opal (IO) Structures

The opal templates were directly infiltrated with precursor solution by two methods. The precursor was formed from a

mixture of IPA, deionized water, and vanadium triisopropoxide oxide ($OV(OCH(CH_3)_2)_3$). Firstly, a mixture of IPA and deionized water was formed in the ratio of 500:1 and a solution of IPA and vanadium triisopropoxide oxide in the ratio of 50:1, this solution was then added to the aqueous IPA for a final IPA:$OV(OCH(CH_3)_2)_3$ ratio of 100:1 and set stirring for ~30 minutes or until clear. This precursor was then directly applied to the opal templates by drop casting under a slight nitrogen overpressure or dip coated at a rate of 200 mm/min × 10 times using an MTI Corporation PTL-MM01 Dip Coater. Sphere removal was performed in a BINDER oven at 300 °C for 12 or 24 h. Removal of spheres was also carried out under UV Ozone for 12 h for the 2D IOs, followed by crystallization at 300 °C for 12 h with no discernible variation in morphology compared to the amorphous material structure.

Instruments and Characterization

Scanning Electron Microscopy (SEM), performed on a Hitachi S-4800 field emission SEM, was used to visualize the in-plane (top layer) ordering of the opals and IOs. Transmission Electron Microscopy (TEM) was conducted at 200 kV using a JEOL JEM-2100 TEM. Raman scattering spectroscopy was performed using a Renishaw InVia Raman Spectrometer with a 514 nm 30mW argon ion laser and spectra were collected using a RenCam CCD camera. The beam was focused onto the samples using a 50× objective lens. X-ray diffraction (XRD) was performed on a Philips Xpert PW3719 diffractometer using Cu Kα radiation. Background subtraction and smoothing was performed using XPert Highscore software, using a bending factor of 17 and quintic polynomial type smoothing respectively.

RESULTS AND DISCUSSION

Methods for 2D and 3D Opal Template Formation

The formation of the multilayer PS or PMMA sphere template on ITO glass by electrophoretic deposition is schematically represented in Fig. 1(a). The resulting polymer sphere deposit is shown in Fig. 1(b) with the (111) plane of the colloidal crystal observed parallel to the substrate. This arrangement has the lowest free energy (maximum packing) for spherical colloids and therefore tends to form preferentially to other planes.

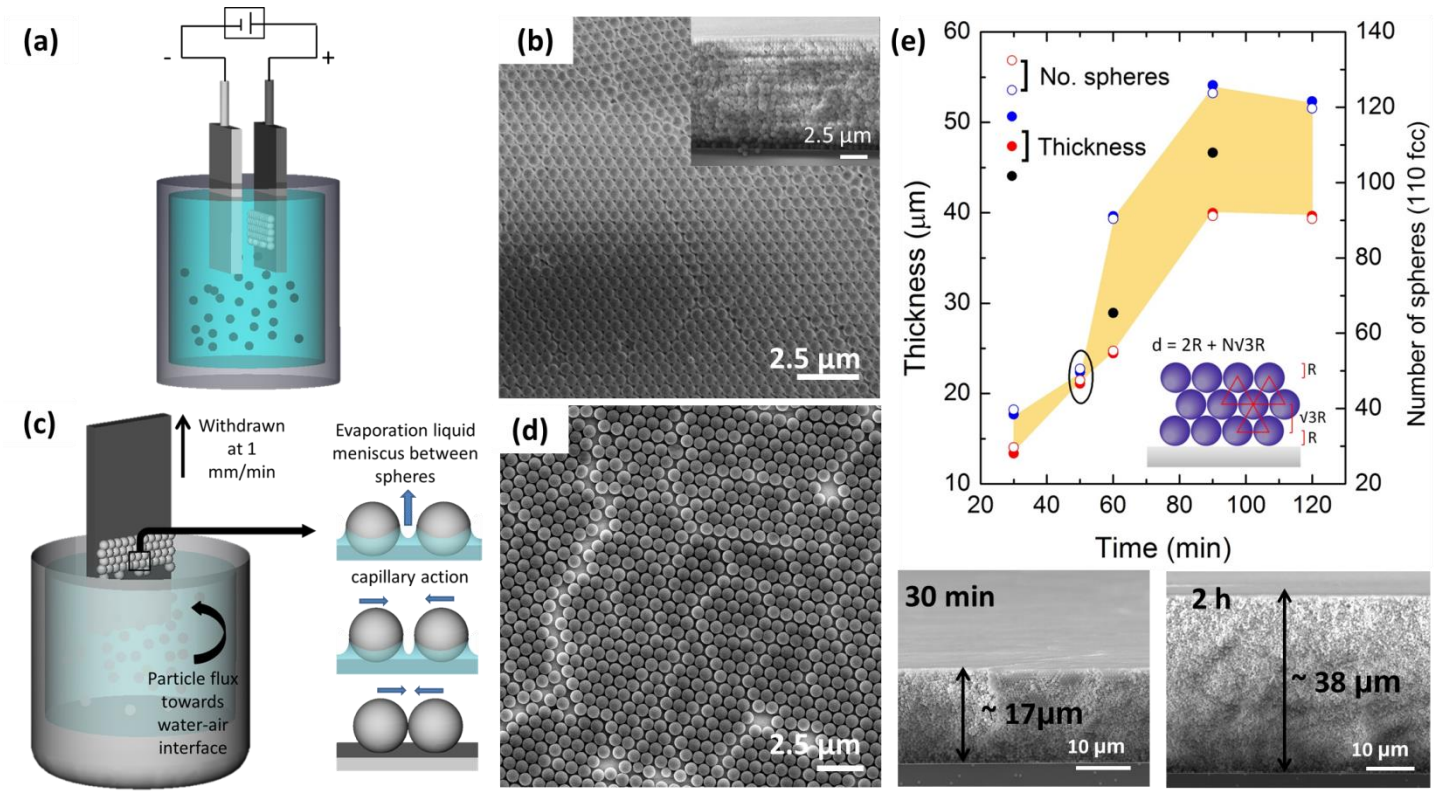

Fig. 1 (a) Schematic of the EPD technique. (b) SEM image of the top surface of the multilayer PS sphere template formed by the EPD technique after 10 min at 3 V. Inset shows cross section indicating multilayer thickness. (c) Schematic of the surfactant assisted dip-coating process for PMMA monolayer formation on gold surfaces. (d) SEM image of the top surface of the 2D monolayer PMMA sphere template with inset showing the monolayer with substrate clearly visible (through voids in the film). (e) Variation in EPD opal thickness as a function of deposition time for sulphated PS spheres on gold-coated silicon substrate.

Electrophoretic deposition of the spheres is possible on any conductive substrate and on a planar surface, the deposited spheres maintain the (111) plane parallel to the substrate as shown in the Supporting Information, Fig. S1. At longer times the ordering can vary between domains due to the speed of sphere deposition and varying E-field strength.

Surfactant-assisted dip coating with PMMA spheres, outlined in the schematic Fig. 1(c), produces a monolayer of PMMA spheres on gold coated silicon substrates, with a (111)-terminated surface shown in Fig. 1(d) similar to EPD deposited 3D opals. The cross-section of a sample prepared by this method (inset of Fig. 1(d)), shows a 2D opal from a single layer of spheres. Usually, gold surfaces quickly turn hydrophobic on interaction with air from any carbonaceous contamination, causing difficulties for ordered sphere deposition. The addition of the SDS surfactant to the solution at a concentration above its critical micelle concentration (CMC) causes the formation of micelles of SDS within solution. These micelles, comprising monomers of SDS with the hydrophilic heads orientated towards the polar solute and hydrophobic tails grouped into a hydrophobic core, allow more time for the spheres to reach an ordered organization at the air-liquid interface by reducing the surface tension, which subsequently reduces the evaporation rate. With the high concentration of 8 mg ml^{-1} (27.7×10^{-3} mol dm^{-3}) of SDS, and consequential formation of micelles in the solution, the horizontal component of the capillary forces between the spheres is increased due to the increase in ionic strength and surface compression of the solution.[59] Micelles then interact with the spheres and the strong lateral forces push the spheres together as an assembly. Using Derjaguin, Landau, Verwey and Overbeek (DLVO) theory[60] and assuming that it is uniquely the SDS in micellular form that causes a separation between otherwise directly touching spheres, it is possible to account for or predict the inter-sphere separation is approximately a single micelle thick between the spheres at maximum packing using SDS just above CMC (see Supporting Information for further details). The spheres' colloidal stability in the presence of SDS at the air-liquid interface within the meniscus and substrate-liquid-air interfaces allows a close-packed ordered monolayer of PMMA spheres that behaves as a 2D diffraction grating.[21]

As the template deposition time increases the deposited spheres will begin to screen the charge from the electrode, weakening the attractive forces induced on the negatively charged spheres by reduction of the electric field influencing the electrophoresis. Therefore, the deposition rate will decrease with time and reach a plateau at very high deposition times.[61] Direct measurements of the thickness of sulphated PS sphere templates on gold-coated silicon substrates for various EPD times at 3 V are shown in Fig. 1 (e), with each dark circle corresponding to a sample from which ~3 measurements were taken across between 3 and 5 different cross-sectional SEM images of the sample. Thickness variations between samples as a result of thickness variations between the top and lower areas on the substrate, contribute to the average values.

At longer deposition times, sphere settlement under gravity can create thickness gradients in the resulting opal deposit, evident by the larger variation between data points in Fig. 1(e) after longer EPD times. At 3 V, an optimum deposition time (thickness) to form a well ordered stable template on gold coated silicon using sulphated PS spheres without thickness gradients is between 30-50 minutes, highlighted by the black oval in Fig. 1(e). The overall mass deposit is directly proportional to the electric field E and the deposition time t, and can also be represented in terms of the opal template thickness d resolved by the number of spheres comprising the deposit as an fcc lattice (see Fig. 1(e) inset), such that $E = V/d$, where $d = (2R + N\sqrt{3}R)$, where V is the applied voltage, R is the sphere radius and N the number of spheres stacked in an fcc lattice viewed along the (110) plane. The E-field is shielded preventing further deposition at 3 V after ~90 mins, which corresponds to a threshold E-field for EPD of $\sim 6.5 \times 10^4$ V/m at a final thickness of ~45 μm or ~103 spheres (Fig. 1(e)) in height.

Methods for 2D and 3D Inverse Opal Formation

Through condensation reactions and hydrolysis the liquid precursor solidifies into a rigid, amorphous V_2O_5 network of material when exposed to moisture in the air, once the added IPA is allowed to evaporate. The application of high temperature should then lead to crystallization of the V_2O_5 material. The method of precursor application and the following heat treatment can greatly influence the morphology and crystallinity of the resulting inverse opals. One of the methods developed in this work is schematically represented in Fig. 2(a). The 100:1 precursor solution was drop cast on to a multi-layered PS sphere template, covered with a cuvette and a using a nitrogen gun, a light flow of nitrogen gas was applied through the top of the cuvette. The template was then heated for 12 h at 300 °C to simultaneously remove the spheres and crystallize the vanadium oxide. Higher temperatures (~450°C) are often used for the crystallization of vanadium oxide from liquid precursors, however, the vanadium oxide was found to grow to sizes and shapes that obscured the inverse opal morphology at those higher temperatures (See Supporting Information, Fig. S2).[62] However, when a lower temperature of 300 °C is used for the longer time of 12 h compared to 5-8 h frequently used at the higher temperature, and the nitrogen assisted infiltration is used as opposed to drop casting by other methods, well-ordered porous structures are achievable as shown in Fig. 3. This lower temperature crystallization is also mentioned as an alternate route to vanadium oxide porous structures by Stein *et al.* but dismissed due to poor ordering within the structure, something we believe is alleviated here by the applied pressure during infiltration and hydrolysis. [62]

A common problem for IO formation is crack propagation in the porous materials which can occur on evaporation of infiltrated solution and shrinkage during sphere removal. Large-scale growth of cracks along large domain boundaries of the starting opal template can lead to islands of IO material that

mirror the grain shapes of the parent opal. The similarity in the shape and directional growth of the cracks and island boundaries in the IO material compared to the grain boundaries in an opal template can be observed in Fig. 2(b) and (c). The application of a steady flow of nitrogen air pressure during solidification increases the infiltration of the precursor through the close packed template as seen in the inset of Fig. 2(b).

A crystalline IO structure is obtained as indicated by the TEM images shown in Figs 2(d) and (e). The nitrogen-containing flow directly above the substrate slows the hydrolysis of the precursor to solid vanadium oxide, improving precursor infiltration through the layers of the template. After 12 h at 300 °C, sphere removal is confirmed by SEM, by which an IO structure comprising two different morphologies is observed, as shown in Fig. 3 (a) and Fig. 3 (b). The variation in morphology and wall thickness can be attributed to a varied degree of precursor infilling before calcination. Used N_2 flow with slight overpressure, while successful in retarding hydrolysis, can apply uneven pressure over the template causing infiltration of more material in certain areas. Crystallization by heating to these two areas for an equal amount of time produced IOs at different stages of crystallization with different morphological characteristics. The characteristic Raman modes at 103, 145, 197, 285, 304, 405, 483, 526, 703, and 995 cm^{-1} are clearly visible for both regions in the Raman scattering spectra taken over both areas of morphology and shown in Fig. 3 (c). These vibrational modes can be indexed to the orthorhombic structure of crystalline V_2O_5 with a space group P*mmn* and D_{2h} point symmetry. Thus, when acoustic modes are ignored, the optical modes (21 in total) are defined as: $\Gamma_{opt} = 7A_g + 7B_{1g} + 3B_{2g} + 4B_{3g} + 3A_u + 3B_{1u} + 6B_{2u} + 6B_{3u}$. In both regions the stretching mode associated with the A_g symmetric vibrations of the short vanadyl V=O bond, with the bond length 1.58 Å, is consistent at 995 cm^{-1}, and the skeleton bent vibration at 145 cm^{-1}, evidence of the layered structure of the V_2O_5, is predominant in both spectra.[63, 64] Variations in the two spectra however are more easily observed in Figs 3 (I)-(III). In these spectra, there are Raman modes visible that are not normally associated with purely crystalline V_2O_5. A low frequency mode at 167 cm^{-1} (Fig. 3(I)) and the higher frequency vibrations at 847, 880 and 936 cm^{-1} (Fig. 3(II)) are found for the IO. Another peak is visible at 1033 cm^{-1} (Fig. 3(III)), particularly in the spectrum of the wider walled morphology (Fig. 3(a)). It is known that several growth mechanisms can occur for different morphologies of vanadium oxide that produce different Raman scattering responses.[65] In some cases, the peaks at ~167, 848, 880 and 936 cm^{-1} have been described as artefactual,[66] but have been observed in several reports involving the synthesis of vanadium oxide structures, as a mixed phase with crystalline V_2O_5.[67] The peaks at 848 and 936 cm^{-1} were previously assigned by Su et al. to a mode of VO_2 and the peak at 167 cm^{-1} discussed as a result of a VO_x layered structure.[65] Several reports have considered these peaks as a characteristic of VO_x nanotubes (VONTs),[67] or a phase seen in VONTs at low annealing temperatures before the nanotube structure is decomposed and re-arranged to form V_2O_5.[68, 69] However, Manning *et al.* observed similar Raman scattering spectra in

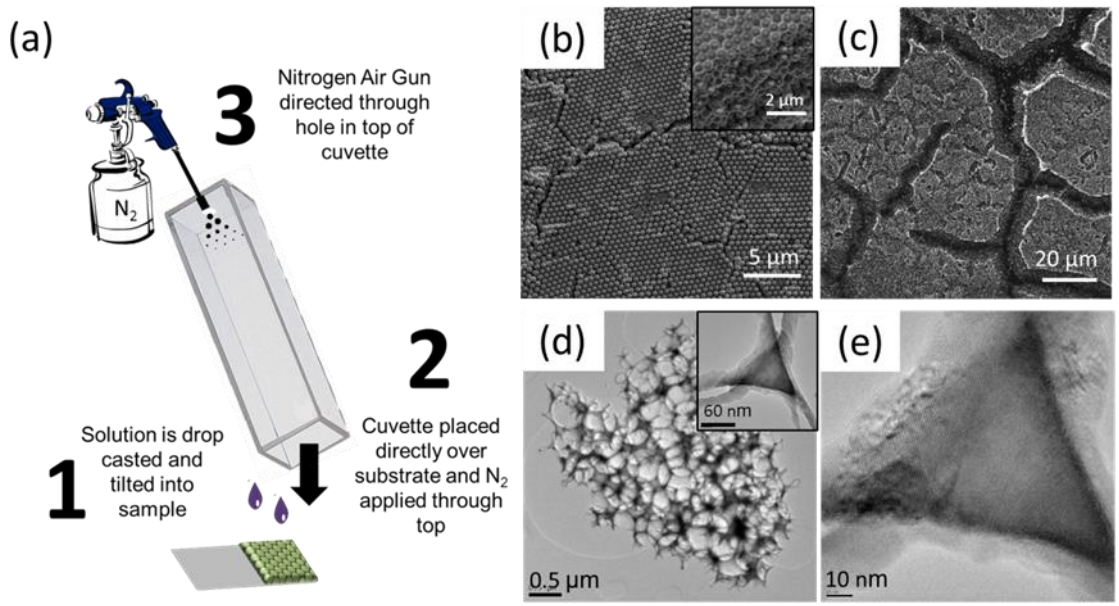

Fig. 2 (a) Schematic diagram of drop casting of precursor solution and the nitrogen-gun-assisted infilling of the template and SEM images of (b) infilled template with inset highlighting the infilling of the precursor to under layers and (c) the overall island morphology due to shrinking of material on drying. TEM image of a section of V_2O_5 thin walled IO with the inset highlighting the distinctive triangular wall region between the macro-pores characteristic of hexagonally ordered structures (f) and of the crystalline planes in the triangular section (e).

V_2O_5 thin films prepared from $VOCl_3$ and from XRD analysis suggests that this mixed phase is V_6O_{13} and $V_2O_{5.69}$ XRD analysis of a sample which is seen to exhibit the foreign Raman peaks, did not yield an XRD pattern conducive with a presence of V_6O_{13}. The pattern, shown in Fig. 3 (f), can be indexed to crystalline orthorhombic V_2O_5 with space group P*mmn* but does not clearly show any alternative phase of vanadium oxide. Some peaks are observed that could represent tetragonal V_2O_5 and these are indicated by the star symbol in Fig. 3(f).

The V-O-V in-plane mode depicted in Fig. 3(II) can theoretically exhibit an antiphase stretch with B_{2g} symmetry. This mode is a pseudo centro-symmetric bending in pristine orthorhombic, layered V_nO_{2n-1}. This mode is predicted at ~848 cm^{-1} when the centro-symmetry is broken and the resulting Raman intensity greatly increases. Therefore the peak at 848 cm^{-1} while present in the Raman scattering response of V_6O_{13}, could also be related to the curved nature of the crystalline structure found in the IO structures[70-72]. The intensities of these

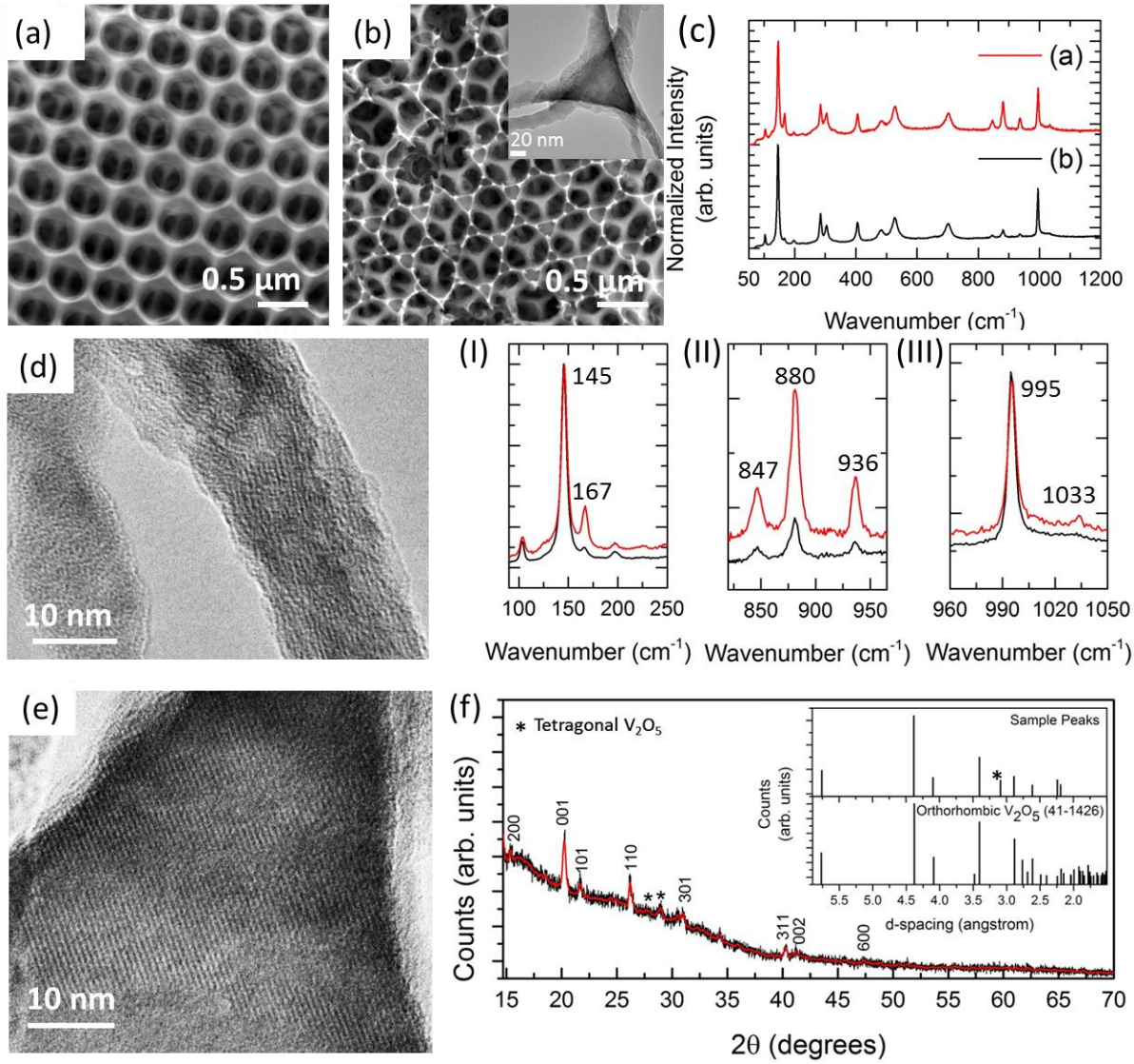

Fig. 3 SEM image of (a) wide walled IO structure and (b) thin walled IO structure seen within the same sample formed from the drop casted 100:1 IPA:$OV(OCH(CH_3)_2)_3$ precursor solution with air-gun assisted infilling and heating for 12 h at 300 °C. (c) Raman scattering for these two different morphologies indicating the greater presence of the minority phase vanadium oxide in the wider walled structure as indicated by the relative intensities of the peaks at (I) 167 cm^{-1} (II) 847, 880, 936 cm-1 and (III) 1033 cm^{-1}. TEM images of IO walls (d) and part of a triangular inter-pore partition (e). (f) XRD pattern of IOs indexed to orthorhombic V_2O_5 with some reflections indexed to tetragonal V_2O_5.

extra peaks, relative to the predominant 145 cm^{-1} and 995 cm^{-1} peaks of the pristine V_2O_5 structure, are lower for defined IO walls, as would be expected if pseudo centrosymmetry is returned for thinner, less curved IO features. Defined and thinner opal walls are in fact linear and not curved (Fig. 3b). Their intensity is markedly increased in the wider walled morphology where we observe a much greater quantity of curved crystalline V_2O_5 regions, but may also include be a mixed oxide phase.

For the multi-layered (3D opal) templates dip-coated with precursor solution, thin, IO structures are observed in many areas. However, the morphology of the material in many areas in this sample is less defined than in the drop cast sample, with the appearance of precursor over-filling in many areas (see inset Fig. 4). Saturation of the top layers, where the precursor completely surrounds individual spheres and hydrolyses before material can penetrate further into the template, could account for this effect. The IO structures are very thin and have smooth, wider walls that appear less uniform in morphology than those seen in the drop cast sample. The relative thinness of this IO structure, seemingly only one layer of material, compared with the drop cast sample can be explained by a lesser degree of template infilling in the absence of the added nitrogen pressure.

Raman scattering data for the multi-layered template dip-coated with the 100:1 precursor solution, shown in Fig. 4, was used to probe the crystal structure and composition simultaneously. The dominant Raman signature observed is identical to the minority phase of vanadium oxide seen in the spectrum in Fig. 3 for the drop-cast IO, most likely V_6O_{13}. The strongest peaks are the vibrations at 167, 848, 880 and 936 cm^{-1} and the peaks associated with crystalline V_2O_5, most importantly the vibrations at 145 and 995 cm^{-1}, associated with long range order within the V_2O_5 planes and the V^{5+}=O bond respectively, are not seen. However, low intensity broad peaks are observed at ~224, 298, 428, and 546 cm^{-1}, which are characteristic of the bending vibrations of V_2O_5. The mode at 224 cm^{-1} is often found only when the modes associated with a frustrated or curved V_2O_5 crystal are found. The peak observed at ~701 cm^{-1} is the classic in-plane antiphase V-O stretching vibration of V_2O_5. The peak observed at ~ 991 cm^{-1} likely represents the stretching vibration of V^{4+}=O bond, before complete oxidation to V^{5+}=O, indicating a presence of more V^{4+} ions than V^{5+}. This Raman signature is identical to that presented by Huotari *et al.* for VO_X-NT, referred to as the VO_X-NT phase (curved or scrolled oxide).[67] The Raman shift associated with bond order = 2 for the V=O bond can be expressed semi-empirically as $\nu = 21349\exp(-1.9176R)$ where R is the bond length.[73] For all 3D and 2D IOs and hollow sphere arrays in this work, this bond is unique to V_2O_5 with a shift close to 1000 cm^{-1} and confirms V_2O_5 formation (see Table S1). Curvature or change in phase must also be those that contain a vanadyl oxygen that is unconstrained at a similar frequency.

Using the same number of drops, the 100:1 precursor solution was drop-cast on a multilayer template and subjected to 300 °C for the longer time of 24 h. The resulting inverted structure can be seen in Fig. 5(a) and at higher magnification in (b). The resulting IOs exhibit long range crystalline order. IOs with well-defined, circular pores are observed with walls that are smooth and somewhat thicker than the thin walled area shown in the sample heated for 12 h (Fig. 3(b)). After 24 h crystallization, the sensitivity of material crystallization to the precursor infilling and resultant IO thickness is also observed, shown in Figs 5 (c)-(f). It is evident through SEM inspection that the wall thickness and the presence of the mixed phase vanadium oxide is not solely dependent on heating time but on precursor hydrolysis and crystallization, with the mixed Raman response (Fig. 5(c)) more prevalent in areas of greater material thickness and better inverted opal structure.

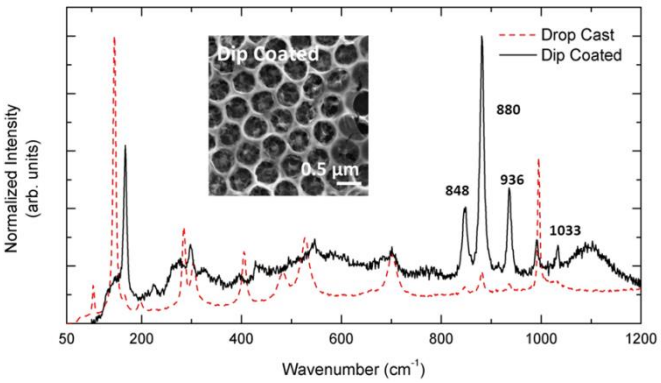

Fig. 4 Raman scattering of dip coated multi-layer template (black line) showing the predominance of the V_6O_{13} phase compared to the spectrum (red dashed line) from the drop cast V_2O_5 IO. Inset SEM image of resulting structure after heat treatment at 300 °C for 12 h of the dip coated precursor.

The change in the wall thickness and thus the periodicity of the IO causes a change in the wavelength of the primary diffraction, or color, as observed in Fig. 5(d,e). Differing degrees of crystallization and spectral purity can be seen in the Raman signatures across the area (Fig.5(c)). Figure 5(f) highlights the 145 cm^{-1} (B_{1g}) mode from all 14 spectra taken along the arrow in Fig. 5(d) at common angles of incidence and diffraction.

This is shown to approach higher intensity (spectra 1-6) where it approaches the 'pink' region indicative of high structural order, and then decreases in intensity (spectra 6-14) as the IO reduces in thickness, characterized by a poorly structured material shown as the brown area in Fig. 5 (d). The same intensity variation is also found in the peak at 995 cm^{-1} (V=O) proving that structural changes, both internal crystalline changes and external macro-structure changes, can correlate to different diffraction in the IOs. In such a scenario, hydrolysing alkoxide may pool and begin to solidify affecting the thickness or concentration of material between the spheres when hydrolysis occurs. Some methods have been proposed where vacuum infiltration can greatly improve the overall infiltration[74]. This however, is suitable for liquid precursors that solidify and crystallize upon heating after full infiltration.

Preventing hydrolysis on surfaces with large surface area is less simplistic. This sensitivity of the Raman characterization to thickness variations and the mixed phase relationship to the amount of precursor present is shown throughout Fig. 5.

The Raman response previously discussed as either associated with VONTs-like curved V_2O_5 or a mixture of V_2O_5 polymorphs are observed in the areas on this sample corresponding to the IO structures with the highest order and regularity, comprised of defined walls and ordered sub-surface.

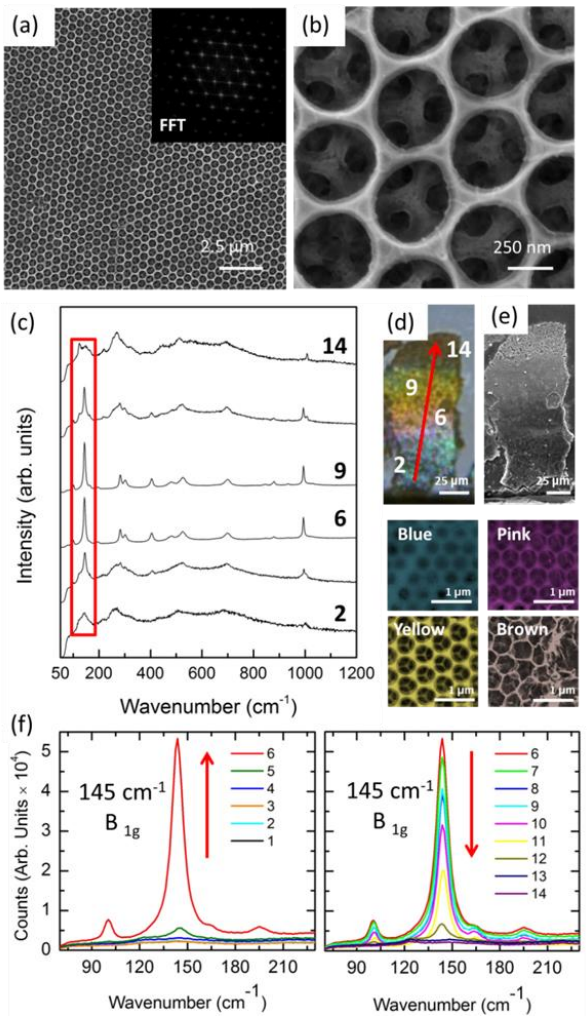

Fig. 5 SEM images (a) and (b) of the structure formed from drop cast 100:1 IPA:OV(OCH(CH$_3$)$_2$)$_3$ precursor solution and N_2-gun assisted infilling with heating for 24 h at 300 °C. (Inset (a)) FFT of the IO structure. (c) Raman scattering data across a region of differing structure and thickness as indicated by accompanying SEM images which correspond to the different colour of light reflected in the optical image in (d) where the red arrow indicates the direction where Raman scattering data was obtained. (e) SEM image of region shown in (d). (f) Evolution of the 145 cm^{-1} peak along the direction indicated by the arrow.

The fact that these peaks are observed in the areas of darkest colour and best defined in structure further suggests these features could be both material and structurally dependent – a higher portion of curved crystalline V_2O_5 contributes to the Raman tensor where the V-O bond polarizability is increased. This occurs when the pseudo-centrosymmtetric structure of the in-plane V-O-V bond is broken due to curvature in the layered structure.

The minority phase peaks, occur in the wider walled morphologies uniquely, pointing further towards their dependence on the arrangement of the vanadium oxide layers in the network of material during hydrolysis and crystallization and an increased level of precursor settlement in those areas. Through TEM, Fig. 3 and Fig. 6, the crystalline nature of all materials is evident, though complete 3D lattice structures are not easily resolved due to the curvature of the materials.

Crystallinity is more distinct in the inter-pore triangular partitions, seen in the TEM images for the drop cast precursor under nitrogen flow and heated for 12 h at 300 °C shown in Fig. 2 and 3 (e), and for the dip coated sample shown in Fig. 6 (a). The IO walls for both the dip coated sample (Fig. 6 (b)) and drop cast samples (Fig. 3(d), Fig. 6(c) and (d)) are shown by TEM imaging to be crystalline regardless of slight variations in crystal structure observed in their Raman responses.

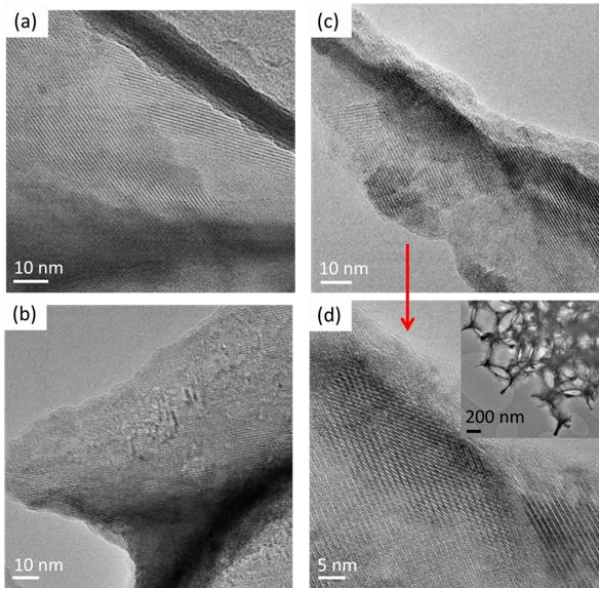

Fig. 6 TEM images indicating the crystalline walls of the IO structures formed from the dip coated multi-layer template (a) and (b) and the drop cast 100:1 IPA:OV(OCH(CH$_3$)$_2$)$_3$ precursor solution and air-gun assisted infilling with heating for 24 h at 300 °C (c) and (d).

In order to determine if the crystallization of the amorphous, hydrolysed material, deposited in the multilayer templates by the two infilling techniques, affected the dimensions of the resulting IOs, line profiles from SEM images of the different structures were taken and are shown in Fig. 7. The templates were formed using 500 nm PS spheres and a plot profile for a

typical top surface of such a template is shown in Fig. 7(a). The peak to peak distance can be taken as a representation of the diameter of the spheres, however, due to secondary electron contrast variations it can more accurately be used as a simple comparison between the plot profile of a closely packed template and the plot profiles taken for the inverted structures shown below this in Fig. 7(b)-(e). All data indicate an average value for the pores very close to the diameter of the spheres (500 nm). The average pore diameter for structures formed after drop casting and 24 h heating at 300 °C is ~505 nm, a broad short intensity peak is also visible in between the more defined peaks of the top surface walls, which are due to the structures visible in the second layer. However, the larger width of these peaks compared with that of the higher intensity peaks indicates a variation (increase) in wall thickness deeper into the structure.

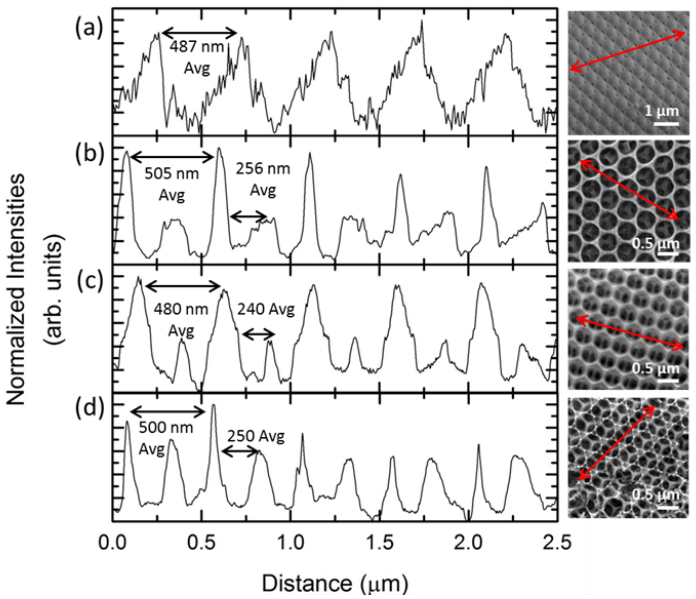

Fig. 7 Plot profiles and corresponding SEM images for a multilayer template of 500 nm spheres deposited by EPD on ITO glass (a) and 100:1 IPA:OV(OCH(CH$_3$)$_2$)$_3$ precursor solution drop cast with N$_2$-gun assisted infilling and heating for 24 h at 300 °C (b) dip coated at a rate of 200 mm/min × 10. (c) Drop cast with N$_2$-gun assisted infilling and heating for 12 h at 300 °C producing the wide walled morphology (d) and thin walled morphology (e).

Comparing Fig. 7(c) and (d) the differences between the two morphologies observed in the drop cast sample with nitrogen assisted infilling, and heating for only 12 h at 300 ºC, can be more closely realized. The average pore diameter for Fig. 7(d) is ~ 480 nm, this is 20 nm less the average diameter calculated for the plot profile of Fig. 7(e) of ~500 nm. This, combined with the broader, high intensity peaks observed in Fig. 7(d) suggests the wall variation is ~20 nm between this morphology and the thinner walled morphology of the highly defined structure shown in Fig. 7(d). However, both these plot profiles produce low intensity peaks, characteristic of the IO walls on the layer beneath the top surface and seen between the pores, exactly midway between the high intensity peaks, (~240 nm and ~250 nm respectively) revealing a very well-ordered structure in both cases.

Examining the plot profiles, it is clearly observed that the superior IOs are attained for the drop cast precursor with hydrolysis under applied nitrogen. However, this method of infiltration can produce areas of uneven infilling which can lead to variations in morphology and crystallinity within the one template outlined in Fig. 3 and Fig. 5. This could be beneficial in applications where variations in material phase, structure or crystallinity are desirable. By controlling the thickness and amount of material deposited, the length and temperature of the applied heat, different phases of the same material can be synthesized in one step and as part of the same structure. Thin walled structures are only attained after sufficient calcination time under temperature, however wider walled structures are also achieved in areas where it is possible more material hydrolysed out of solution. This is also likely controllable by varying the ratio of IPA to undiluted precursor, a smaller ratio will produce more crystalline V_2O_5 for a given area, but in this case hydrolysis will occur faster on exposure to air and moisture. These samples present possibilities for further investigations into the origin of the peaks sometimes seen in VONTs and their structural dependence, the arrangement of the vanadium oxide layers in the wider-walled IOs may be comparable to the walls of VONTs, unlike the mono-layered or thin-walled IOs.

2D Monolayer Vanadium Oxide IOs and Hollow Sphere Arrays

Monolayer templates of PMMA spheres were formed by surfactant assisted dip-coating as outlined in our previous work, [21] whereby the spheres, due to micellular interactions, exhibit better order at higher withdrawal rates. This produced order similar to that of a 2D diffraction grating as shown by the light scattered normal to the surface when incident at 60° (see Supporting Information Fig. S3). 2D monolayer templates prepared in this way were then infiltrated using the same two methods used for the multilayer samples. The resulting formations can be seen if Fig. 8 (a-e). Due to the thin nature of the monolayer templates the precursor, when drop cast and subjected to nitrogen air flow for infiltration assistance, pooled beneath the spheres between the substrate surface and sphere resulting in basin-like structures shown in plan-view in Fig. 8(a) with the cross-section shown in Fig. 8(d). Hydrolysis within a confined inter-sphere spacing solidifies into a solid but at the expense of a reduced volume, causing defects within the structure.

The over-filling effect discussed for the multi-layer dip-coated sample (summarised schematically in Fig. 8(b)) was more pronounced in 2D monolayer-templated structures, leading to alternative structure formation. In such cases an array of hollow spheres of V_2O_5 are formed as seen in Fig. 8(c) and Fig. 8(e). We postulate that hollow sphere 2D arrays could form as a consequence of the instability of PMMA in IPA, leading to their breakdown with each successive dip-coating in

conjunction with continuing material hydrolysis. This would account for the absence of the spheres after heating without appreciable breakdown in the individual crystalline hollow spheres. Alternatively, the spheres may decompose with evolving CO and CO_2 escaping through voids in the structure. Future research may provide routes for optimizing single and multilayer hollow sphere arrays. Both the drop cast and dip coated monolayer templates when heated at 300 °C for 12 h produced crystalline V_2O_5 as evidenced by the Raman scattering shown in Fig. 8(f). The characteristic peaks of the 145 cm^{-1} and 995 cm^{-1}, indicative of the layered structure and V=O short-length bond are well defined. Mixed phases of vanadium oxide are not observed in either of the monolayer IOs. This provides further evidence that template thickness influences crystallization; 12 h at 300 °C is insufficient for complete crystallization to orthorhombic V_2O_5 but is sufficient for these thinner material deposits in 2D IOs.

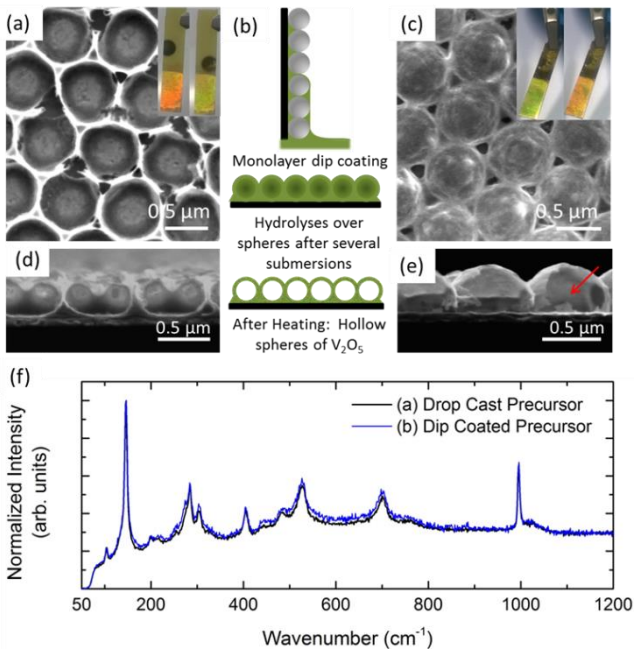

Fig. 8 SEM image of the structure formed when precursor is drop cast with nitrogen assisted infilling and heated at 12 h for 300 °C (b) Schematic outlining the dip coating of a monolayer PMMA template with precursor solution and (c) SEM image of a monolayer PMMA template when dip coated at a rate of 200 mm/min × 10 times (d) Cross section of the structure shown in (a). (e) Cross section of the hollow spheres shown in (c). The red arrow indicates the hollow internal structure. Insets of (a) and (c) show optical image of the visible diffraction from these 2D structures. (f) Raman scattering of both (a) and (b) confirming V_2O_5 crystal structure.

A monolayer template dipped at a rate of 150 mm/min × 8 into precursor solution and subjected to UV Ozone for an extended period of 12 h, produced 2D IO structures of amorphous vanadium oxide, shown in Fig. 9(a), i.e. removing the sphere template without crystallizing the vanadium oxide precursor. This results in a high quality, ordered 2D vanadium oxide IO with smooth walls. After heating for 12 h at 300 °C to crystallize the material, the structure shows negligible deformation, shown in Fig. 9 (b) and is confirmed as crystalline V_2O_5 as indicated by the Raman scattering spectrum shown in Fig. 9(c) thus indicating UV Ozone is a viable route for amorphous IO structures that do not experience further growth or modifications to overall arrangement during heating and crystallization. Due to the monolayer nature of the template, infilling is possible after fewer coats. These structures have extremely thin walls due to the ratio of alkoxide in the IPA diluted precursor and subsequent low filling factor after only one dip at a very high withdrawal rate of 150 mm/min (see Supporting Information, Fig. S4).

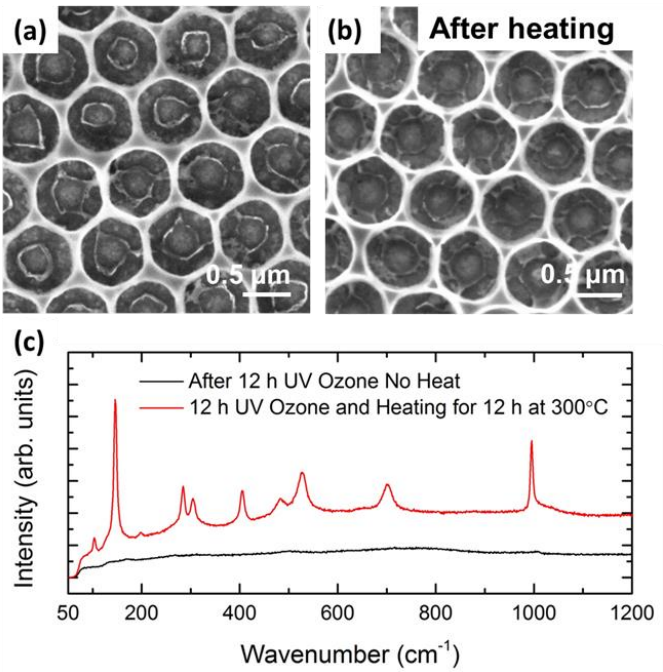

Fig. 9 SEM images of (a) amorphous vanadium oxide after dip coating with 100:1 IPA:$OV(OCH(CH_3)_2)_3$ precursor at a rate of 150 mm/min × 8 times and treated with UV Ozone for 12 h and (b) following heating for 12 h at 300 °C. (c) Raman scattering spectrum of the crystallized vanadium oxide following the heat treatment compared with the amorphous spectrum of the material after UV Ozone treatment only.

The thickness of the multilayer samples and the close-packed arrangement presented a difficulty in complete infiltration of precursor and the resulting IO can often lose up to 70% in thickness after sphere removal. This could be reduced with further study into concentration and type of precursor solution. However, we have shown that the synthesis of ordered IOs of crystalline vanadium oxide are possible when using liquid precursor and infilling is assisted by some applied pressure and slowed hydrolysis. Crystallization is then performed at a lower temperature and a longer time than most other methods so as to prevent over-growth of the vanadium oxide and loss of the ordered structure.

Conclusions

This work has demonstrated how 2D and 3D opals and corresponding vanadium oxide IOs can be formed from electrophoretically deposited templates and subsequent infilling methods. The formation and crystallization of the 2D and 3D V_2O_5 inverse opals was followed in detail through Raman scattering and we demonstrated that the type of precursor deposition and subsequent treatment and removal of the sphere template greatly influences the morphology, crystallinity and phase of the resulting IOs structures. The ability to form high quality 2D IOs using UV Ozone removal of PMMA sphere templates was also demonstrated. Where rapid hydrolysis can occur, the formation of 2D arrays of crystalline hollow spheres of V_2O_5 is possible using iterative coating of opal templates. These methods provide viable routes for amorphous IO materials that optically diffract as a grating that can later be crystallized without major changes to the IO structure, and can likely be generalized to any template structure that uses polymeric templates capable of decomposition under UV-ozone exposure. The infiltration methods described here have the advantage of simplicity and low cost, with samples subjected to less strenuous synthetic methods, compared to other methods, such as CVD, ALD, PLD or electro-deposition, which is desirable for up-scaled charge storage, sensing, electrochromic and optoelectronic applications involving ordered or porous materials that behave as photonic crystals or 2D diffraction gratings. Very large area templating on planar and curved surfaces on metallic surfaces augers well for applications that require a conductive contact to the functional porous materials.

Acknowledgements

E. A., M. O., and C. G. acknowledge the support of the Irish Research Council under awards RS/2010/2920, RS/2010/2170, and RS/2011/797, respectively. This research has received funding from the Seventh Framework Programme FP7/2007-2013 (Project STABLE) under grant agreement n°314508. C.O.D. acknowledges support from Science Foundation Ireland under award no. 07/SK/B1232a-STTF11, the UCC Strategic Research Fund and from the Irish Research Council New Foundations Award. This work was also supported by Science Foundation Ireland under the National Access Programme (NAP 417).

References and Notes

Department of Chemistry, University College Cork, Cork, Ireland, and Micro & Nanoelectronics Centre, Tyndall National Institute, Lee Maltings, Cork, Ireland. Email: c.odwyer@ucc.ie; Tel: (0)21 4902732; Fax: (0)21 4274097.

Electronic Supplementary Information (ESI) available: SEM characterization of 3D photonic crystal opals formed on gold-coated silicon, glass and ITO substrates, light scattering spectra of 2D opal formation on gold-coated silicon, SEM images of 2D IO formation from dip-coating, and DLVO theory estimates of micellular SDS thickness on polymer spheres. See DOI:

1. A. Stein and R. C. Schroden, *Curr. Opin. Solid State Mater. Sci.*, 2001, **5**, 553-564.
2. P. Vukusic and J. R. Sambles, *Nature*, 2003, **424**, 852-855.
3. M. Osiak, H. Geaney, E. Armstrong and C. O'Dwyer, *J. Mater. Chem. A*, 2014.
4. A. Stein, B. E. Wilson and S. G. Rudisill, *Chem. Soc. Rev.*, 2013, **42**, 2763-2803.
5. C. López, *Adv. Mater.*, 2003, **15**, 1679-1704.
6. P. V. Braun, *Chem Mater*, 2013, **26**, 277-286.
7. B. Hatton, L. Mishchenko, S. Davis, K. H. Sandhage and J. Aizenberg, *Proc. Natl. Acad. Sci. U. S. A.*, 2010, **107**, 10354-10359.
8. J. Aizenberg, D. A. Muller, J. L. Grazul and D. R. Hamann, *Science*, 2003, **299**, 1205-1208.
9. L. Lu, J. D. Joannopoulos and M. Soljačić, *Phys. Rev. Lett.*, 2012, **108**, 243901.
10. Y. Liu, F. Qin, Z.-Y. Wei, Q.-B. Meng, D.-Z. Zhang and Z.-Y. Li, *Appl. Phys. Lett.*, 2009, **95**, 131116.
11. C. Geng, T. Wei, X. Wang, D. Shen, Z. Hao and Q. Yan, *Small*, 2014, **10**, 1668–1686.
12. H. Zhang and P. V. Braun, *Nano Lett.*, 2012, **12**, 2778-2783.
13. J. H. Pikul, H. G. Zhang, J. Cho, P. V. Braun and W. P. King, *Nat. Commun.*, 2013, **4**, 1732.
14. H. Zhang, X. Yu and P. V. Braun, *Nat. Nanotechnol.*, 2011, **6**, 277-281.
15. G. von Freymann, V. Kitaev, B. V. Lotsch and G. A. Ozin, *Chem. Soc. Rev.*, 2013, **42**, 2528-2554.
16. M. Pichumani, P. Bagheri, K. M. Poduska, W. Gonzalez-Vinas and A. Yethiraj, *Soft Matter*, 2013, **9**, 3220-3229.
17. O. D. Velev, K. Furusawa and K. Nagayama, *Langmuir*, 1996, **12**, 2374-2384.
18. A. L. Rogach, N. A. Kotov, D. S. Koktysh, J. W. Ostrander and G. A. Ragoisha, *Chem. Mater.*, 2000, **12**, 2721-2726.
19. B. van Duffel, R. H. A. Ras, F. C. De Schryver and R. A. Schoonheydt, *J. Mater. Chem.*, 2001, **11**, 3333-3336.
20. W. Khunsin, A. Amann, G. Kocher-Oberlehner, S. G. Romanov, S. Pullteap, H. C. Seat, E. P. O'Reilly, R. Zentel and C. M. S. Torres, *Adv. Funct. Mater.*, 2012, **22**, 1812-1821.
21. E. Armstrong, W. Khunsin, M. Osiak, M. Blömker, C. M. S. Torres and C. O'Dwyer, *Small*, 2014, **10**, 1895-1901.
22. B. Mandlmeier, N. K. Minar, J. M. Feckl, D. Fattakhova-Rohlfing and T. Bein, *J. Mater. Chem. A*, 2014, **2**, 6504-6511.
23. D. L. Ma, Z. Y. Cao, H. G. Wang, X. L. Huang, L. M. Wang and X. B. Zhang, *Energy Environ. Sci.*, 2012, **5**, 8538-8542.
24. G. Collins, M. Blömker, M. Osiak, J. D. Holmes, M. Bredol and C. O'Dwyer, *Chem. Mater.*, 2013, **25**, 4312-4320.
25. V. Dusastre, *Nat. Mater.*, 2013, **12**, 1080.
26. B. Kang and G. Ceder, *Nature*, 2009, **458**, 190-193.
27. J.-M. Tarascon and M. Armand, *Nature*, 2011, **414**, 359-367.
28. A. Vu, Y. Qian and A. Stein, *Adv. Energy Mater.*, 2012, **2**, 1056-1085.
29. H. Zhang and P. V. Braun, *Nano Letters*, 2012, **12**, 2778-2783.
30. A. Stein, *Nat. Nanotechnol.*, 2011, **6**, 262-263.

31. D. Wei, M. R. J. Scherer, C. Bower, P. Andrew, T. Ryhänen and U. Steiner, *Nano Lett.*, 2012, **12**, 1857-1862.
32. G. S. Armatas and M. G. Kanatzidis, *Science*, 2006, **313**, 817-820.
33. S. C. Warren, L. C. Messina, L. S. Slaughter, M. Kamperman, Q. Zhou, S. M. Gruner, F. J. DiSalvo and U. Wiesner, *Science*, 2008, **320**, 1748-1752.
34. J. Bao, X. Zhang, L. Bai, W. Bai, M. Zhou, J. Xie, M. Guan, J. Zhou and Y. Xie, *Journal of Materials Chemistry A*, 2014, **2**, 10876-10881.
35. J. Zhu, L. Cao, Y. Wu, Y. Gong, Z. Liu, H. E. Hoster, Y. Zhang, S. Zhang, S. Yang, Q. Yan, P. M. Ajayan and R. Vajtai, *Nano Letters*, 2013, **13**, 5408-5413.
36. I. Bita, J. K. W. Yang, Y. S. Jung, C. A. Ross, E. L. Thomas and K. K. Berggren, *Science*, 2008, **321**, 939-943.
37. J. Aizenberg, P. V. Braun and P. Wiltzius, *Phys. Rev. Lett.*, 2000, **84**, 2997-3000.
38. C. G. Granqvist, *Thin Solid Films*, 2014, **564**, 1-38.
39. M. A. Kats, D. Sharma, J. Lin, P. Genevet, R. Blanchard, Z. Yang, M. M. Qazilbash, D. N. Basov, S. Ramanathan and F. Capasso, *Appl. Phys. Lett.*, 2012, **101**, -.
40. M. A. Kats, R. Blanchard, S. Zhang, P. Genevet, C. Ko, S. Ramanathan and F. Capasso, *Physical Review X*, 2013, **3**, 041004.
41. R. O. Prum, T. Quinn and R. H. Torres, *J. Exp. Biol.*, 2006, **209**, 748-765.
42. Z. Li, Z. Hu, J. Peng, C. Wu, Y. Yang, F. Feng, P. Gao, J. Yang and Y. Xie, *Adv. Funct. Mater.*, 2014, **24**, 1821-1830.
43. F. Nicholas, M. P. Sean, W. H. Mark and S. S. N. Bharadwaja, *Journal of Physics D: Applied Physics*, 2009, **42**, 055408.
44. G. T. Kim, J. Muster, V. Krstic, J. G. Park, Y. W. Park, S. Roth and M. Burghard, *Appl. Phys. Lett.*, 2000, **76**, 1875-1877.
45. T. Zhai, H. Liu, H. Li, X. Fang, M. Liao, L. Li, H. Zhou, Y. Koide, Y. Bando and D. Golberg, *Adv. Mater.*, 2010, **22**, 2547-2552.
46. M. S. Whittingham, *Chem. Rev.*, 2004, **104**, 4271-4301.
47. C. O'Dwyer, V. Lavayen, D. A. Tanner, S. B. Newcomb, E. Benavente, G. González and C. M. S. Torres, *Adv. Funct. Mater.*, 2009, **19**, 1736-1745.
48. Y. Wang, K. Takahashi, K. Lee and G. Z. Cao, *Adv. Funct. Mater.*, 2006, **16**, 1133-1144.
49. D. Vernardou, D. Louloudakis, E. Spanakis, N. Katsarakis and E. Koudoumas, *New J. Chem.*, 2014, **38**, 1959-1964.
50. K. J. Takeuchi, A. C. Marschilok, S. M. Davis, R. A. Leising and E. S. Takeuchi, *Coord. Chem. Rev.*, 2001, **219–221**, 283-310.
51. R. A. Leising and E. S. Takeuchi, *Chem. Mater.*, 1994, **6**, 489-495.
52. C. K. Chan, H. Peng, R. D. Twesten, K. Jarausch, X. F. Zhang and Y. Cui, *Nano Lett.*, 2007, **7**, 490-495.
53. J. S. Sakamoto and B. Dunn, *J. Mater. Chem.*, 2002, **12**, 2859-2861.
54. D. R. Rolison, J. W. Long, J. C. Lytle, A. E. Fischer, C. P. Rhodes, T. M. McEvoy, M. E. Bourg and A. M. Lubers, *Chem. Soc. Rev.*, 2009, **38**, 226-252.
55. S. Tepavcevic, H. Xiong, V. R. Stamenkovic, X. Zuo, M. Balasubramanian, V. B. Prakapenka, C. S. Johnson and T. Rajh, *ACS Nano*, 2012, **6**, 530-538.
56. L. Li, U. Steiner and S. Mahajan, *J. Mater. Chem.*, 2010, **20**, 7131-7134.
57. M. R. J. Scherer, L. Li, P. M. S. Cunha, O. A. Scherman and U. Steiner, *Adv. Mater.*, 2012, **24**, 1217-1221.
58. D. Rehnlund, M. Valvo, K. Edström and L. Nyholm, *J. Electrochem. Soc.*, 2014, **161**, D515-D521.
59. M. Marquez and B. P. Grady, *Langmuir*, 2004, **20**, 10998-11004.
60. E. J. W. Verwey and J. T. G. Overbeek, *Theory of the Stability of Lyophobic Colloids*, Elsevier, Amsterdam, 1948.
61. L. Besra and M. Liu, *Prog. Mater. Sci.*, 2007, **52**, 1-61.
62. B. T. Holland, C. F. Blanford, T. Do and A. Stein, *Chem. Mater.*, 1999, **11**, 795-805.
63. R. Baddour-Hadjean, J. P. Pereira-Ramos, C. Navone and M. Smirnov, *Chem. Mater.*, 2008, **20**, 1916-1923.
64. C. Glynn, D. Thompson, J. Paez, G. Collins, E. Benavente, V. Lavayen, N. Yutronic, J. D. Holmes, G. Gonzalez and C. O'Dwyer, *J. Mater. Chem. C*, 2013, **1**, 5675-5684.
65. Q. Su, C. K. Huang, Y. Wang, Y. C. Fan, B. A. Lu, W. Lan, Y. Y. Wang and X. Q. Liu, *J. Alloys Compd.*, 2009, **475**, 518-523.
66. A. G. Souza Filho, O. P. Ferreira, E. J. G. Santos, J. Mendes Filho and O. L. Alves, *Nano Lett.*, 2004, **4**, 2099-2104.
67. J. Huotari, J. Lappalainen, J. Puustinen and A. Lloyd Spetz, *Sens. Actuators, B*, 2013, **187**, 386-394.
68. V. Lavayen, C. O'Dwyer, G. Cárdenas, G. González and C. M. Sotomayor Torres, *Mater. Res. Bull.*, 2007, **42**, 674-685.
69. C. O'Dwyer, V. Lavayen, S. B. Newcomb, M. A. Santa Ana, E. Benavente, G. González and C. M. Sotomayor Torres, *J. Electrochem. Soc.*, 2007, **154**, K29-K35.
70. F. Krumeich, H. J. Muhr, M. Niederberger, F. Bieri, B. Schnyder and R. Nesper, *J. Am. Chem. Soc.*, 1999, **121**, 8324-8331.
71. C. O'Dwyer, G. Gannon, D. McNulty, D. N. Buckley and D. Thompson, *Chem. Mater.*, 2012, **24**, 3981-3992.
72. G. Gannon, C. O'Dwyer, J. A. Larsson and D. Thompson, *J. Phys. Chem. B*, 2011, **115**, 14518-14525.
73. F. D. Hardcastle and I. E. Wachs, *J. Phys. Chem.*, 1991, **95**, 5031-5041.
74. X. Chen, Z. Li, J. Ye and Z. Zou, *Chem. Mater.*, 2010, **22**, 3583-3585.

